Fast single image super-resolution using estimated low-frequency k-space data in MRI

Jianhua Luo [a], Zhiying Mou [b], Binjie Qin [c,*], Wanqing Li [d], Feng Yang [e], Marc Robini [f], Yuemin Zhu [f]

[a] School of Aeronautics and Astronautics, Shanghai Jiao Tong University, 200240, China
[b] China National Aeronautical Radio Electronics Research Institute, Shanghai 200233, China
[c] School of Biomedical Engineering, Shanghai Jiao Tong University, Shanghai 200240, China
[d] School of Computer Science and Software Engineering, University of Wollongong, NSW 2522, Australia
[e] School of Computer and Information Technology, Beijing Jiao Tong University, China
[f] University of Lyon; CNRS UMR 5220; Inserm U1206; INSA Lyon, Creatis, France

ARTICLE INFO

ABSTRACT

Purpose: Single image super-resolution (SR) is highly desired in many fields but obtaining it is often technically limited in practice. The purpose of this study was to propose a simple, rapid and robust single image SR method in magnetic resonance (MR) imaging (MRI).
Methods: The idea is based on the mathematical formulation of the intrinsic link in k-space between a given (modulus) low-resolution (LR) image and the desired SR image. The method consists of two steps: 1) estimating the low-frequency k-space data of the desired SR image from a single LR image; 2) reconstructing the SR image using the estimated low-frequency and zero-filled high-frequency k-space data. The method was evaluated on digital phantom images, physical phantom MR images and real brain MR images, and compared with existing SR methods.
Results: The proposed SR method exhibited a good robustness by reaching a clearly higher PSNR (25.77dB) and SSIM (0.991) averaged over different noise levels in comparison with existing edge-guided nonlinear interpolation (EGNI) (PSNR=23.78dB, SSIM=0.983), zero-filling (ZF) (PSNR=24.09dB, SSIM=0.985) and total variation (TV) (PSNR=24.54dB, SSIM=0.987) methods while presenting the same order of computation time as the ZF method but being much faster than the EGNI or TV method. The average PSNR or SSIM over different slice images of the proposed method (PSNR=26.33 dB or SSIM=0.955) was also higher than the EGNI (PSNR=25.07dB or SSIM=0.952), ZF (PSNR=24.97dB or SSIM=0.950) and TV (PSNR=25.70dB or SSIM=0.953) methods, demonstrating its good robustness to variation in anatomical structure of the images. Meanwhile, the proposed method always produced less ringing artifacts than the ZF method, gave a clearer image than the EGNI method, and did not exhibit any blocking effect presented in the TV method. In addition, the proposed method yielded the highest spatial consistency in the inter-slice dimension among the four methods.
Conclusions: This study proposed a fast, robust and efficient single image SR method with high spatial consistency in the inter-slice dimension for clinical MR images by estimating the low-frequency k-space data of the desired SR image from a single spatial modulus LR image.

1. Introduction

Magnetic resonance (MR) imaging (MRI) is an important diagnostic technique in routine clinical practice due to its powerful, flexible and non-invasive imaging characteristics. However, MRI faces the persistent problem of limited spatial resolution. To enhance the spatial resolution in MRI, most methods can be distinguished:

acquisition [1,2] and image processing schemes. Recently, the combination strategy integrating the two schemes also has been proposed [3]. The acquisition scheme aims to observe smaller details by trying to achieve optimal compromise between various factors such as acquisition time, signal-to-noise ratio (SNR), field of view, image size, type of sequences, and type of tissues. Unfortunately, most of these techniques are based on the acquisition of multiple low resolution (LR) images with small shifts (or rotations) which is time consuming and therefore not applicable for typical clinical settings. The image processing methodology called the high- or

* Corresponding author.
  E-mail address: bjqin@sjtu.edu.cn (B. Qin).

super-resolution (HR or SR) reconstruction recover a SR image from a single or multiple acquired low-resolution images to improve or enhance the visibility of image details [1–9]. The main drawback of multiple image SR is that acquiring multiple images of the same object is often difficult, if not impossible in certain situations. Furthermore, the multiple image SR is highly dependent on the estimation accuracy of the motions between the multiple LR observations by image registration [10], which gets more unstable and difficult in real-world applications due to the different objects in the same clinical scene having different and complex motions [11]. For these reasons, most recent works advocate the use of single image SR for MR imaging. Obviously, it is more challenging.

Currently, there are three categories of single image SR methods with their advantages and limitations: interpolation-based [12–17], reconstruction-based [8,9,19–23], and example learning-based methods [25–30]. Note that ideas of methods in different categories might have been combined. For instance, some interpolation-based [17] methods might also involve the strategies of reconstruction-based and learning-based methods. Interpolation methods are straightforward and widely exploited in signal processing and medical imaging [12]. They directly project (or up-sample) the initial LR image onto an HR grid and estimate the missing pixel values using parametric and nonparametric interpolation functions, such as bicubic, B-spline interpolation function and edge-directed interpolation [18]. Traditionally, interpolation of medical imaging datasets to higher image resolution has not been thought of as a possible way for potentially increasing anatomical detail. However, recent researches [13] indicate that conventional interpolation method can be successfully applied to diffusion weighted imaging datasets for mining anatomical details that are normally seen only at higher resolutions. Usually, the interpolation functions assume some smoothness prior in the image space, which are not valid in inhomogeneous areas. Hence conventional interpolation methods usually result in blurred edges and textures as well as artifacts in lines. To solve these problems, some recent state-of-the-art interpolation methods have been proposed in SR, using edge-guided nonlinear interpolation (EGNI) [14] to preserve sharp edges and reduce ring artifacts, employing reproducing kernel Hilbert space [15] to estimate coefficients of the basis and redundant functions for SR images at any finer grids, or using steering kernel regression [16] as well as local structure prior [17] to construct the image interpolation model. However, these methods may introduce edge diffusion or haloing artifacts in the recovered images. Usually, these new methods enhance the single image SR performance but sacrifice the computational efficiency and simplicity that conventional interpolation methods have. For instance, although the resulting SR image by smooth regression or nonlinear interpolation based method is pleasing, there exists huge computational overhead because all the smooth kernel regression [16] or edge-guided nonlinear interpolation [14] have to be iteratively calculated for each pixel of input LR image.

Reconstruction-based SR methods are based upon imaging degradation model and solve an ill-posed inverse problem of deblurring, up-sampling, and denoising for a SR image. To reduce edge artifacts and estimate the SR detail, reconstruction-based SR methods incorporate the constraints or the prior knowledge to model a regularized cost function with a data-fidelity term in optimization. The data-fidelity term usually penalizes the difference between the degraded SR image and observed LR image, while the typical regularization terms in the cost function include edge gradient [19], patch-based nonlocal regularization [8], structure-preserving constraint [9], total-variation (TV) regularization [20–22], low rank regularization [22], and non-local steering kernel regression based regularization [23]. However, reconstruction-based SR algorithms are still clumsy at introducing important high-frequency details into the output SR image when solving the computationally hard optimization problems. Generally, the unavoidable blur generated by the initial interpolation together with the lack of high-frequency details in the LR input image limits their effectiveness to small magnification factors, their performance degrades rapidly if the magnification factor is large [24].

The example learning-based algorithms utilize different machine learning techniques [25–30] to learn the mapping relationship between the LR and SR image patches from external low- and high-resolution exempla pair in training datasets and then transform the input LR image into the desired SR image using this priori knowledge. The learnt relationship between SR and LR training details sets the quality of the SR image. Therefore, training data needs to be relevant and large enough to learn useful structures for the kind of input LR image. However, these methods are usually computationally expensive and can produce obvious artifacts and unwanted noises into the synthesized SR image if with unsuitable training samples.

Integrating advantages of computational efficiency, reconstruction fidelity and large magnification ratio, as well as without using external training data, in this paper we propose a novel and fast single image SR method for MRI, namely low-frequency k-space data estimation (LFE for short). On the one hand, it adopts the reconstruction consistency constraints in an average imaging model to ensure consistency between the reconstructed SR images and the input SR image; on the other hand, it utilizes a weighted complex-valued modulation function in frequency domain expressing the intrinsic link in k-space between a given (modulus) LR MR image and the desired SR MR image, which enables us to increase resolution with large magnification ratio. More specifically, in the single image SR MRI, a pixel (or voxel) of LR images is equivalent to averaging pixels (or voxels) of the SR image. This averaging nature determines that the LR image preserves well low-frequency components but erases high-frequency components of the SR image. Therefore, as long as the low-frequency k-space data of the SR image can be obtained from LR images, the SR image can then be reconstructed by means of partial k-space image reconstruction techniques such as zero filling the non-acquired k-space data. This strategy enables us to have a more rapid and efficient SR method while largely reducing ringing artifact problem compared with the SR method solely based on zero-filling (ZF) [31] in the Fourier space.

This fundamentally different SR method is based on first estimating, from a single spatial modulus LR image, the low-frequency k-space data of the desired SR image, and then reconstructing the latter by simply inverse Fourier transform of the partially weighted k-space data formed of the estimated low-frequency and zero-filled high-frequency k-space data. Without producing the edge diffusion, haloing and blocking artifacts, the proposed weighted k-space data-based method is much more stable and rapid than the edge-guided interpolation-based [14] and TV [20,21] regularization-based methods. The rest of this paper is organized as follows. Section 2 presents the proposed LFE method. Experimental results and analysis are presented in Section 3. Finally, Section 4 concludes the paper.

2. Methods

2.1. Theory of low-frequency estimation

First note that in what follows all the images in question are discrete images. An observed LR MR image $g_l(i,j), i,j \in \chi_l = \{0, 1, \ldots, N-1\}$ can be considered resulting from a desired SR MR image $g(i,j), i,j \in \chi = \{0, 1, \ldots, sN-1\}$ via averaging process with a magnification factor s. The latter designates s times the resolution (e.g., $s = 2$ means that the image size goes from $N \times N$ to $2N \times 2N$). In other words, the value of $g_l(i,j)$ at a pixel is the average of $g(si+a, sj+b)$

in a $s \times s$ neighborhood. The link between the LR and SR images can mathematically be formulated as

$$g_l(i,j) = \frac{1}{s^2} \sum_{a=0}^{s-1} \sum_{b=0}^{s-1} g(si+a, sj+b) \qquad (1)$$

where $a, b \in \{0, 1, \ldots, s-1\}$ are the relative positions in the neighborhood along $x-$ and $y-$ axes, respectively.

The k-space or spectral data of the SR image $g(i,j), i, j \in \{0, 1, \ldots, sN-1\}$ is given by

$$G(k_i, k_j) = \mathcal{F}[g(i,j)], \quad k_i, k_j \in \left\{-\frac{sN}{2}, -\frac{sN}{2} + 1, \ldots, \frac{sN}{2} - 1\right\} \qquad (2)$$

where $\mathcal{F}[\cdot]$ designates Fourier transform.

The k-space data of the SR image $g(i,j)$ in the low-frequency space $k_i, k_j \in \left\{-\frac{N}{2}, -\frac{N}{2} + 1, \ldots, \frac{N}{2} - 1\right\}$ can be expressed as (see the derivation details in appendix)

$$\begin{aligned} G(k_i, k_j) &= \mathcal{F}[g(i,j)], \quad k_i, k_j \in \left\{-\frac{N}{2}, -\frac{N}{2} + 1, \ldots, \frac{N}{2} - 1\right\} \\ &= \sum_{i=0}^{N-1} e^{\frac{-2\pi i k_i \sqrt{-1}}{N}} \sum_{a=0}^{s-1} e^{\frac{-2\pi a k_i \sqrt{-1}}{sN}} \\ &\quad \times \left[\sum_{j=0}^{N-1}\left[\sum_{b=0}^{s-1} g(si+a, sj+b) e^{\frac{-2\pi b k_j \sqrt{-1}}{sN}}\right] e^{\frac{-2\pi j k_j \sqrt{-1}}{N}}\right] \end{aligned} \qquad (3)$$

In the above equation, $g(si+a, sj+b)$ with $a, b \in \{0, 1, \ldots, s-1\}$ and $i, j \in \{0, 1, \ldots, N-1\}$ represents the gray-level value at a pixel and $\frac{1}{s^2} \sum_{a=0}^{s-1} \sum_{b=0}^{s-1} g(si+a, sj+b)$ the averaged gray-level value in a neighborhood of the desired unknown SR image. According to Eq. (1), such averaged value of the SR image is equal to the LR image pixel value $g_l(i,j), i, j \in \{0, 1, \ldots, N-1\}$. We now back-project a pixel value of the LR image $g_l(i,j)$ to a neighborhood of the SR image to have an approximate estimation of the pixel value of the SR image in that neighborhood. We then have

$$g(si+a, sj+b) \approx g_l(i,j), \quad \forall a, b = 0, 1, \ldots, s-1 \text{ and } i, j = 0, 1, \ldots, N-1 \qquad (4)$$

Thus, to estimate the k-space data of the desired $G(k_i, k_j)$ in the low-frequency space $k_i, k_j \in \left\{-\frac{N}{2}, -\frac{N}{2} + 1, \ldots, \frac{N}{2} - 1\right\}$ (of size $N \times N$), we use Eq. (4) to approximate $g(si+a, sj+b)$ by the pixel value of the LR image $g_l(i,j)$ in Eq. (3). The low-frequency k-space data of the SR image $g(i,j)$ can then be approximately expressed as (see the derivation details in appendix)

$$\begin{aligned} G(k_i, k_j) &\approx \sum_{i=0}^{N-1} e^{\frac{-2\pi i k_i \sqrt{-1}}{N}} \sum_{a=0}^{s-1} e^{\frac{-2\pi a k_i \sqrt{-1}}{sN}} \left[\sum_{j=0}^{N-1}\left[\sum_{b=0}^{s-1} g_l(i,j) e^{\frac{-2\pi b k_j \sqrt{-1}}{sN}}\right] e^{\frac{-2\pi j k_j \sqrt{-1}}{N}}\right] \\ &= \left(\sum_{a=0}^{s-1} e^{\frac{-2\pi a k_i \sqrt{-1}}{sN}}\right)\left(\sum_{b=0}^{s-1} e^{\frac{-2\pi b k_j \sqrt{-1}}{sN}}\right) G_l(k_i, k_j), \\ k_i, k_j &\in \left\{-\frac{N}{2}, -\frac{N}{2} + 1, \ldots, \frac{N}{2} - 1\right\} \end{aligned} \qquad (5)$$

where

$$G_l(k_i, k_j) = \sum_{i=0}^{N-1} \sum_{j=0}^{N-1} e^{\frac{-2\pi(ik_i + jk_j)\sqrt{-1}}{N}} g_l(i,j), \quad k_i, k_j \in \left\{-\frac{N}{2}, -\frac{N}{2} + 1, \ldots, \frac{N}{2} - 1\right\} \qquad (6)$$

which represents the k-space data of the LR image.

The approximation in Eq. (5) comes from the approximation in Eq. (4). Such approximation is somewhat like the idea of data consistency. It consists in regarding a pixel value of the observed (known) LR image as the averaged value of the desired (estimated) SR image in SR reconstruction. Eq. (5) shows that the low-frequency k-space data $k_i, k_j \in \left\{-\frac{N}{2}, -\frac{N}{2} + 1, \ldots, \frac{N}{2} - 1\right\}$ of the desired SR image $g(i,j)$ can be estimated from the k-space data $G_l(k_i, k_j)$ of the observed LR image after modulation by some function. By denoting this function as

$$W_s(k_i, k_j) = \left(\sum_{a=0}^{s-1} e^{\frac{-2\pi a k_i \sqrt{-1}}{sN}}\right)\left(\sum_{b=0}^{s-1} e^{\frac{-2\pi b k_j \sqrt{-1}}{sN}}\right),$$
$$k_i, k_j \in \left\{-\frac{N}{2}, -\frac{N}{2} + 1, \ldots, -\frac{N}{2} - 1\right\} \qquad (7)$$

the k-space data in the low-frequency space $k_i, k_j \in \left\{-\frac{N}{2}, -\frac{N}{2} + 1, \ldots, \frac{N}{2} - 1\right\}$ of the super-resolved SR image is then given by

$$G(k_i, k_j) \approx W_s(k_i, k_j) G_l(k_i, k_j), \quad k_i, k_j \in \left\{-\frac{N}{2}, -\frac{N}{2} + 1, \ldots, \frac{N}{2} - 1\right\} \qquad (8)$$

$W_s(k_i, k_j)$ is a complex-valued function. Its modulus and phase are illustrated in Fig. 1. The estimation error of the k-space data of the SR image in the low frequencies $k_i, k_j \in \left\{-\frac{N}{2}, -\frac{N}{2} + 1, \ldots, \frac{N}{2} - 1\right\}$ using Eq. (8) stems from the fact that the gray-level value of the SR image has been replaced by the averaged value in a neighborhood. Such neighborhood averaging suppresses high-frequency components but in general does not alter seriously low-frequency components of the SR image. Therefore, the average value replacing will induce only small estimation errors on low-frequency k-space data.

2.2. Reconstruction method

Based on the theory of low-frequency k-space data estimation presented above, we now show how to reconstruct a desired SR image $g(i,j), i, j \in \chi$ from an observed LR image $g_l(i,j), i, j \in \{0, 1, \ldots, N-1\}$. Keep in mind that the k-space data of the SR image is $G(k_i, k_j)$, $k_i, k_j \in \Omega = \left\{-\frac{sN}{2}, -\frac{sN}{2} + 1, \ldots, \frac{sN}{2} - 1\right\}$. According to Eq. (8), its k-space data (estimated) in the low-frequency subspace $\Omega_l = \left\{-\frac{N}{2}, -\frac{N}{2} + 1, \ldots, \frac{N}{2} - 1\right\}$ is given by $W_s(k_i, k_j) G_l(k_i, k_j)$, but its k-space data in the high-frequency subspace $k_i, k_j \notin \Omega_l$ is missing. Therefore, to reconstruct the SR image, we fill the high-frequency k-space $\Omega - \Omega_l$ with zeros, thus leading to the following full k-space data of the SR image $g(i,j), i, j \in \chi$

$$G(k_i, k_j) \text{ SINC}(k_i, k_j) \approx \begin{cases} G_l(k_i, k_j) W_s(k_i, k_j), & k_i, k_j \in \Omega_l \\ 0, & k_i, k_j \in \Omega - \Omega_l \end{cases} \qquad (9)$$
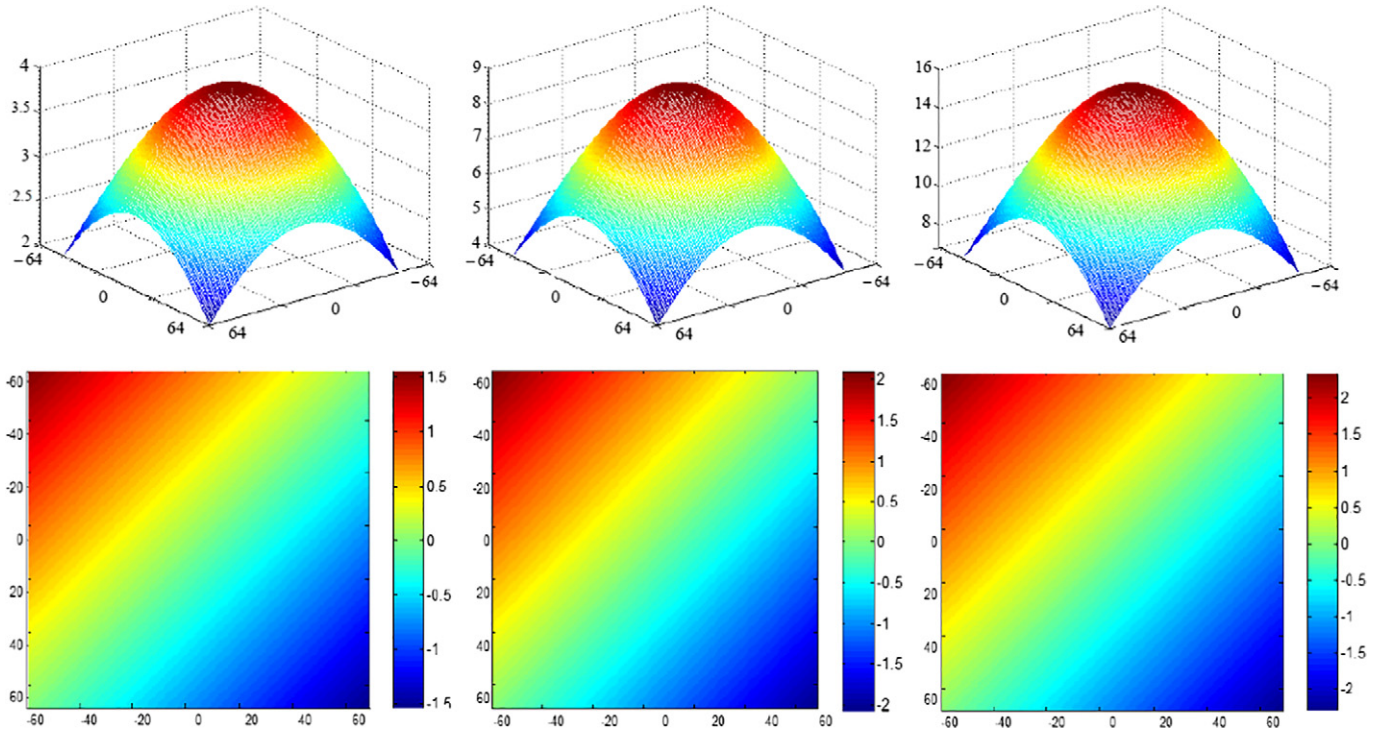
with

$$\text{SINC}(k_i, k_j) = \begin{cases} 1, & k_i, k_j \in \Omega_l \\ 0, & k_i, k_j \in \Omega - \Omega_l \end{cases} \qquad (10)$$

The SR image $g(i,j), i, j \in \chi$ can finally be approximately reconstructed by

$$g(i,j) \approx \mathcal{F}^{-1}[G(k_i, k_j) \text{ SINC}(k_i, k_j)], \quad i, j \in \chi \qquad (11)$$

where $\mathcal{F}^{-1}[\cdot]$ designates inverse Fourier transform.

Fig. 1. The modulus (top row) and phase (bottom row) maps of the modulation function $W_s(k_i, k_j)$ for three different values of the magnification factor $s = 2, 3, 4$ (from left to right).

Eq. (11) shows that we can very simply reconstruct a desired SR image by inverse Fourier transform of the k-space data formed of the estimated low-frequency and zero-filled high-frequency k-space data. Therefore, it is extremely simple and rapid. We call such approximate reconstruction the LFE method, since it is essentially based on low-frequency k-space data estimation.

It is important to underline that the product $G_l(k_i, k_j)W_s(k_i, k_j)$ in Eq. (9) is fundamentally different from the apodization windows often used in MRI to reduce Gibbs ringing (i.e., truncation artifacts). Indeed, any (real-valued) smooth apodization window function (e.g. Hamming or Hanning window) can be used to multiply it with the acquired k-space data, but this is at the cost of reducing resolution because the windowing function destroys original k-space data. In contrast, the modulation function in Eq. (9) is not an arbitrary smoothing function; it is a complex-valued function that is different following the magnification factor s (in Eq. (7)). The modulation function expresses the intrinsic link in k-space between a given (modulus) LR image and the desired SR image (Eq. (8)), which enables us to increase resolution.

Fig. 2 schematizes the process of reconstructing an SR image $g(i, j)$ from a given LR image $g_l(i, j)$ through estimating the low-frequency k-space data $W_s(k_i, k_j)G_l(k_i, k_j)$ of $g(i, j)$ and using inverse Fourier transform.

3. Experiments and results

To evaluate the proposed LFE method, digital phantom images, physical phantom MR images and real brain MR images were used. The digital phantom image is Sheep-Logan head image of size 256 × 256, to which we add Gaussian noises of different levels from 1 to 15. The Gaussian noises have zero mean and the standard deviations (STD) being changed in the range of $1/255, 2/255, \ldots, 15/255$, i.e., noise level 1 is equal to STD $= 1/255$, noise level 2 is equal

to STD $= 2/255$, etc. Note that adding noise to the spatial image is equivalent to adding the noise to k-space data according to the principle of Fourier transform (or mimicking the remained noise in the k-space). The real brain MR images contain eight volumes: three volumes from our laboratory and five volumes corresponding to case 1 to case 5 of the MRI public datasets [33][1]. The three MRI volume sets with voxel resolution $1.0 \times 1.0 \times 1.0$ represent respectively transverse, coronal and sagittal volumes of 256 slices with size 256 × 256. The five public datasets represent five transverse volumes (pixel resolution 0.9375 × 0.9375, slice thickness 1.3 mm, 124 slices of size 256 × 256).

The proposed method was also compared with the aforementioned ZF [31], EGNI [14] and TV [20–22] methods. The ZF SR method consists of first taking the initial k-space data of the original LR image as the low-frequency k-space data of the desired SR image, filling zeros in the high-frequency k-space of the latter, regarding the so obtained k-space data as the full k-space data of the desired SR image, and taking inverse Fourier transform of the full k-space data to obtain the SR image. So, the ZF SR method amounts to taking $W_s(k_i, k_j) = 1, k_i, k_j \in \Omega_l$ in Fig. 2.

The EDNI [14] is a representative SR interpolation method based on directional filtering and data fusion. In this method, for a pixel to be interpolated, two observation sets are defined in two orthogonal directions, and each set produces an estimate of the pixel value. Such interpolation technique can preserve edge sharpness and avoid ringing artifacts. In all the simulation experiments, LR images were obtained by merging 4 neighboring pixels of the reference image.

The TV method [20–22] is based on the following regularization. Let a desired SR MR image $g(i, j), i, j \in \chi = \{0, 1, \ldots, sN - 1\}$ to

---
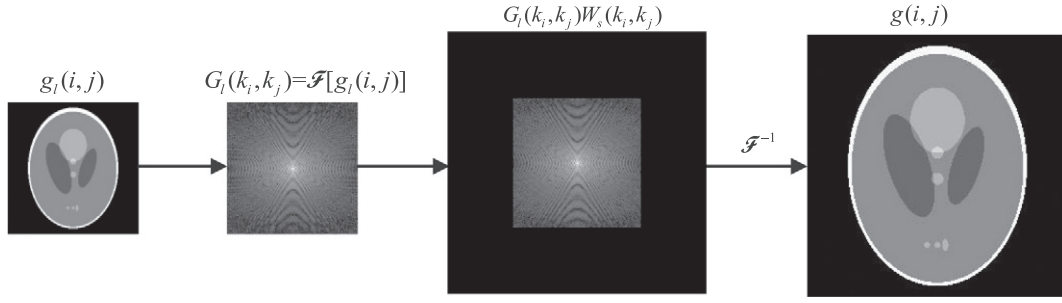
Fig. 2. Scheme of reconstructing an SR image from a single LR image through estimating its low-frequency k-space data.

be reconstructed from an observed LR MR image $g_l(i,j), i,j \in \chi_l = \{0, 1, \ldots, N-1\}$, the SR image $g(i,j)$ is obtained by resolving

$$\begin{cases} \min_{g(i,j)} \text{ TV}(g(i,j)) \\ \text{subject to } \|h(g(i,j)) - g_l(i,j)\|^2 = \sigma^2 \end{cases} \quad (12)$$

where σ is the standard deviation of the noise in $g_l(i,j)$ and $h(g(i,j)) = \frac{1}{s^2} \sum_{a=0}^{s-1} \sum_{b=0}^{s-1} g(si+a, sj+b)$.

To evaluate the robustness of the proposed method to noise, the peak signal-to-noise ratio (PSNR) was calculated that is defined by

$$\text{PSNR} = 20 \lg \frac{P_k}{\text{RSME}} \quad (13)$$

where $P_k = \max_{i,j=0,1,\ldots,N} \left\{ |g(i,j)| \right\}$ and $\text{RMSE} = \sqrt{\frac{1}{N^2} \sum_{i=0}^{N-1} \sum_{j=0}^{N-1} [g(i,j) - g_0(i,j)]^2}$ with $g_0(i,j)$ and $g(i,j)$ indicating respectively the reference and estimated images.

To further quantify the quality of the reconstructed SR images, the structural similarity (SSIM) [32] index and the image error were also calculated. The SSIM index that allows us to evaluate the structural quality of the reconstructed SR image with respect to the reference image is given by

$$\text{SSIM}(g, g_0) = \frac{8 \mu_g \mu_{g_0} \sigma_g \sigma_{g_0} \sigma_{g,g_0}}{(\mu_g^2 + \mu_{g_0}^2)(\sigma_g^2 + \sigma_{g_0}^2)(\sigma_g + \sigma_{g_0})} \quad (14)$$

where $\mu_g = \frac{1}{N^2} \sum_{i=0}^{N-1} \sum_{j=0}^{N-1} g(i,j)$, $\mu_{g_0} = \frac{1}{N^2} \sum_{i=0}^{N-1} \sum_{j=0}^{N-1} g_0(i,j)$, $\sigma_g = \sqrt{\frac{1}{N^2} \sum_{i=0}^{N-1} \sum_{j=0}^{N-1} [g(i,j) - \mu_g]^2}$, $\sigma_{g_0} = \sqrt{\frac{1}{N^2} \sum_{i=0}^{N-1} \sum_{j=0}^{N-1} [g_0(i,j) - \mu_{g_0}]^2}$, $\sigma_{g,g_0} = \sqrt{\frac{1}{N^2} \sum_{i=0}^{N-1} \sum_{j=0}^{N-1} [g(i,j) - \mu_g][g_0(i,j) - \mu_{g_0}]}$.

The higher SSIM is, the higher the similarity between the reconstructed SR and reference images.

The image error map between the reconstructed SR and reference images is defined by

$$e(i,j) = g(i,j) - g_0(i,j) \quad (15)$$

It is the most direct and most intuitive way to evaluate edge distortion and artifacts in the reconstructed SR images.

3.1. Influence of noise

With the Sheep-Logan head phantom image, the ground-truth is known. So, we took it as reference image and added to it the noise of levels 1 to 15, thus yielding reference images whose corresponding PSNRs are given in Table 1. The PSNR (left) and SSIM (right) curves of the SR images reconstructed using the EGNI, ZF, TV and proposed LFE methods are plotted in Fig. 3 as a function of noise level. Noise impacts the four methods, and the accuracy of the three methods decreased as the noise increased. But, the proposed LFE method has clearly higher PSNRs than both ZF and EGNI methods over the whole range of noise levels. The PSNR of the ZF method is always slightly better than the EGNI method. More globally, the average PSNR over the whole range of noise levels of the EGNI, ZF, TV, and LFE methods are respectively 23.78, 24.09, 24.54 and 25.77 dB. The best performance of the proposed LFE method is confirmed by the comparison of the SSIM scores between the four methods. Their average SSIM values over the whole range of noise levels are respectively 0.983, 0.985, 0.987, 0.991 indicating that the LFE always achieves the highest SSIM.

Fig. 4 shows the super-resolution reconstruction results and the corresponding image errors with the noise level 2. The LR image (of size 128 × 128) in the left bottom of Fig. 4 is obtained after merging 4 neighboring pixels in the reference image (of size 256 × 256, in Fig. 4 (a)). The SR images (in Fig. 4 (b)–(e)) reconstructed from the LR image show that the EGNI method generates blurring, the ZF method presents ringing artifacts, the TV method yields very smooth image but exhibiting blocking effect at edges, the LFE method is the closest to the reference image. Their zoomed versions (Fig. 4 (g) to (j)) show clearly their difference. Compared with the other methods (Fig. 4 (k)–(m)) in terms of image error, the LFE method (Fig. 4 (n)) presents the least visible object pattern, thus inducing the smallest errors on edge information.

3.2. Reconstruction results on physical phantom image

With the physical phantom reference image (in Fig. 5 (a)), the corresponding LR image of size 256 × 256 in the left bottom of Fig. 5 is obtained after merging 4 neighboring pixels in the reference image. The SR images of size 512 × 512 in Fig. 5 (b)–(e) were reconstructed from the LR image using respectively the EGNI, ZF, TV and LFE methods. Compared with the zoomed version of reference image (in Fig. 5 (f)), the zoomed versions (Fig. 5 (g)–(j)) of the SR reconstruction results clearly show that the SR image obtained using the EGNI

Table 1
PSNRs of reference images (dB).

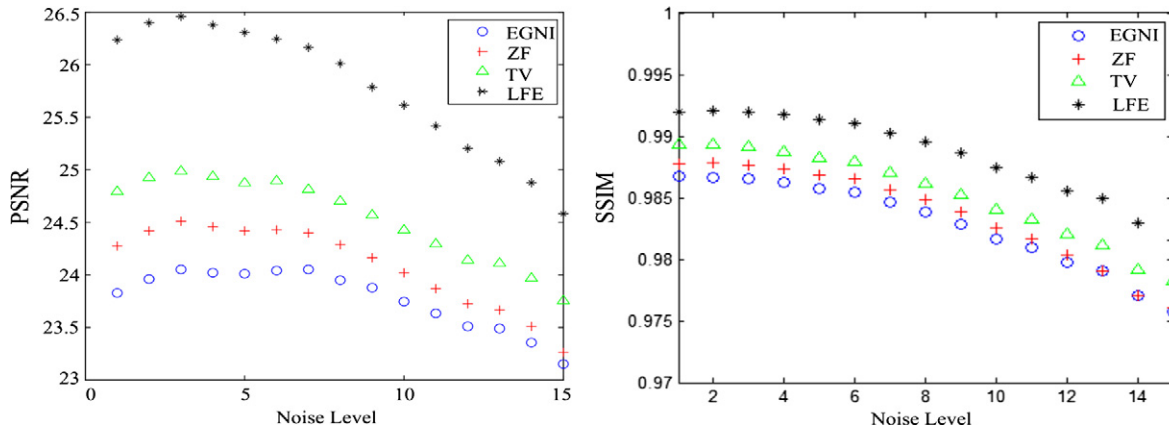| Noise level	1	2	3	4	5	6	7	8	9	10	11	12	13	14	15
PSNRs	48.10	42.07	38.56	36.03	34.13	32.52	31.18	30.04	28.99	28.08	27.25	26.50	25.81	25.17	24.56

Fig. 3. Variation of PSNRs in dB (left) and SSIM (right) as a function of noise level of SR images reconstructed using the EGNI, ZF, TV and LFE methods.

method looks blurred (Fig. 5 (g)), the ZF method displays ringing artifacts (Fig. 5 (h)), the TV method yields over-smoothing and blocking effect in particular on the raster (Fig. 5 (i)), and the LFE (Fig. 5 (j)) generates the best quality image showing a rather clean aspect without blurring and largely reduced ringing artifacts. This visual assessment is clearly confirmed in the image error maps (Fig. 5 (k)–(n)), among which the image errors induced by the proposed LFE method (Fig. 5 (n)) are not only the smallest but also demonstrate the least visible object structures.

3.3. Reconstruction results on real brain MR images

We have applied different SR methods to the eight real brain volumes mentioned above. Figs. 6 to 8 and Table 2 represent the results on the transverse slices of the in-house data. Table 3 gives the comparison between different SR methods on the eight real brain volumes in terms of PSNRs and SSIMs.

Fig. 6 gives the super-resolution reconstruction results on the real brain axial MR images presenting variable anatomical structures, in which the PSNR and SSIM curves of the SR images reconstructed by the EGNI, ZF, TV and LFE methods are plotted as a function of slices. By fixing any slice, we observe that the PSNR of the LFE method is always clearly higher than that of the TV method but largely higher than that of the EGNI or ZF method. The TV method has better PSNR performance than the EGNI and ZF methods that have rather close PSNR values. The EGNI method is nevertheless slightly better than the ZF method. Across all the slices, the LFE method always keeps higher PSNR whatever the variation in anatomical structure of the slices. This is confirmed in terms of SSIM criterion, the LFE always having the highest SSIM value.
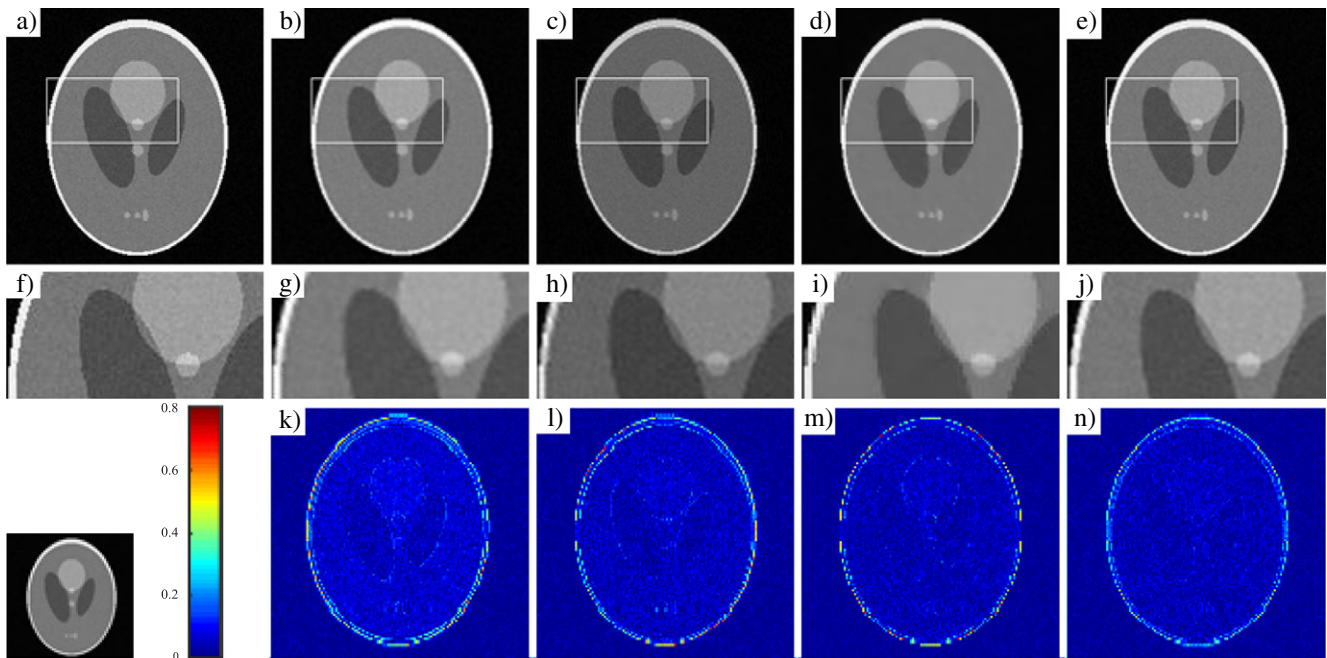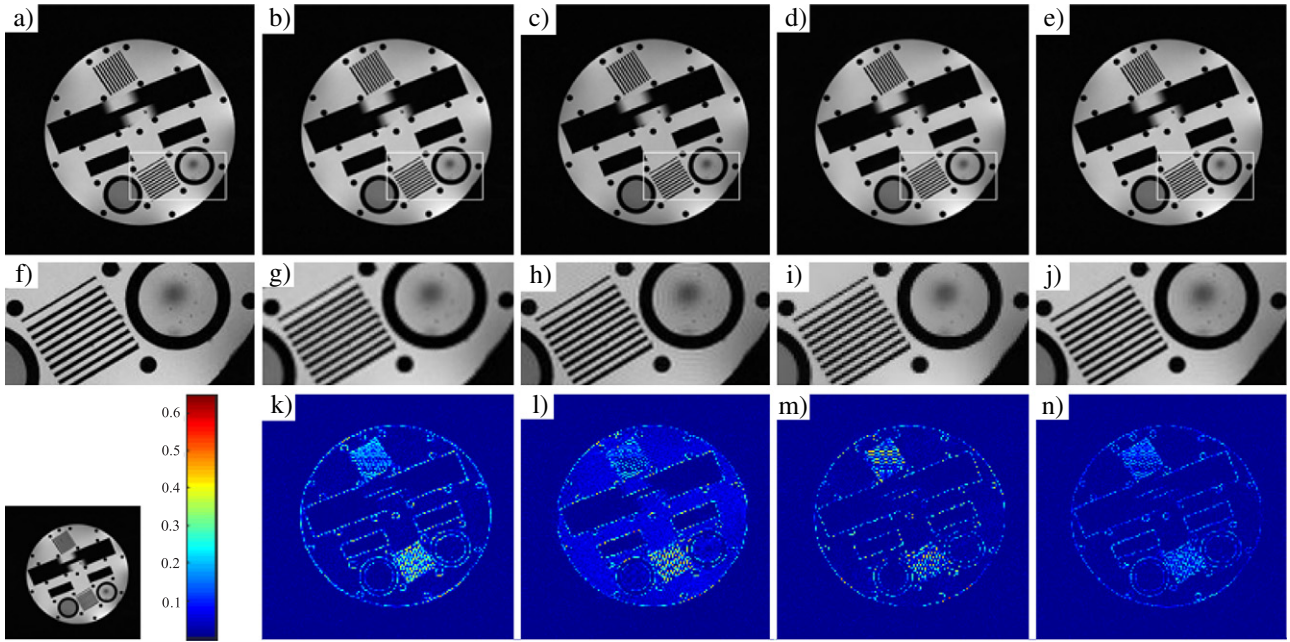

Fig. 4. Super-resolution reconstruction results and the corresponding image error maps with the noise level 2. (a) Reference image. (b)–(e) represent the SR images obtained using respectively the EGNI, ZF, TV and LFE methods. (f)–(j) are the zoomed versions of the boxed regions in (a)–(e), respectively. The corresponding image errors between the reconstructed SR images ((b)–(e)) and the reference image ((a)) are given in (k)–(n).
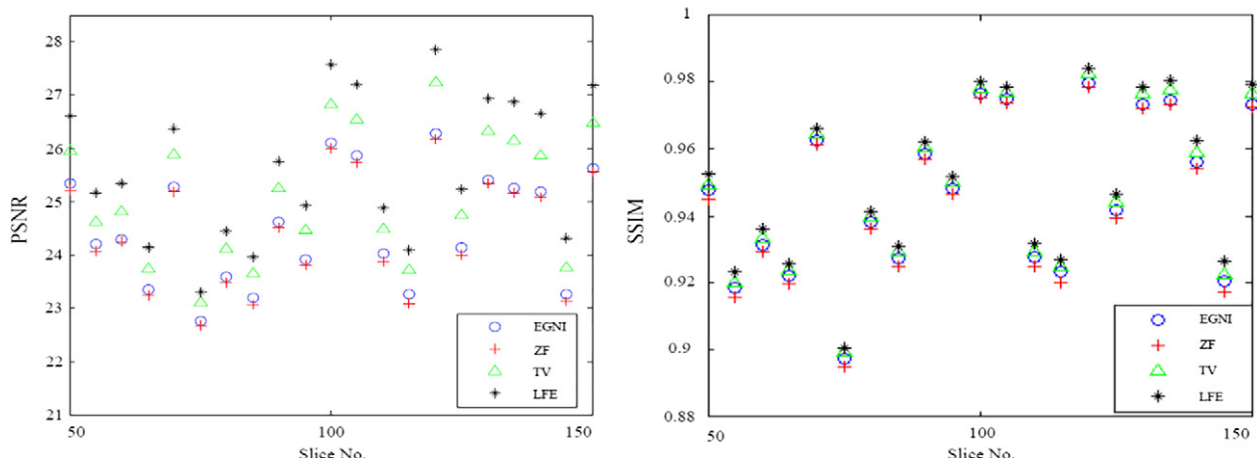
Fig. 5. Super-resolution reconstruction results and the corresponding image errors on the physical phantom image. (a) Reference image. (b)–(e) represent the SR images obtained using the EGNI, ZF, TV and LFE methods, respectively. (f)–(j) are the corresponding zoomed versions of the boxed regions in (a)–(e). The corresponding image errors between the reconstructed SR images ((b)–(e)) and the reference image ((a)) are given in (k)–(n).

More globally, over all the slices, the average PSNR of the EGNI, ZF, TV and LFE are respectively about 25.07, 24.97, 25.7 and 26.33 dB, and their corresponding average SSIMs are respectively 0.952, 0.950, 0.953 and 0.955.

To visually assess the differences between the four methods, we choose to illustrate in Fig. 7 the results on the 100th slice of the brain MR volume. The sizes of the LR image (in the left bottom of Fig. 7) is 128 × 128. The size of reference and the reconstructed SR images (Fig. 7 (a)–(e)) is 256 × 256. Based on the zoomed version of the reference image, the differences between the four methods can be more easily observed in the zoomed versions of their respective boxed regions (Fig. 7 (g) to (j)). The image with the EGNI method looks blurred (Fig. 7 (b) or (g)), the image with the ZF method exhibits serious ringing artifacts (Fig. 7 (c) or (h)), the image with the TV method yields over-smoothing and rather visible blocking effect

(Fig. 7 (d) or (i)), and the image with the LFE method has the best quality (Fig. 7 (e) or (j)). Again, in terms of image error displayed in the Fig. 7 (k)–(n), the LFE method has the smallest error and the least visible anatomical patterns among the four methods.

In Fig. 8 we illustrate super-resolution reconstruction results when the magnification factor s is superior to 2. Clearly, as the magnification factor increases, the advantage of the proposed LFE method becomes more and more evident (Fig. 8 (e) and (j)). When the magnification factor was increased to 4, the proposed LFE method still provided a fairly clean and sharp image (Fig. 8 (j)) in comparison with the EGNI method (Fig. 8 (g)) where the interpolation of magnification factor 4 was achieved by two successive interpolations of magnification factor 2, or the ZF method (Fig. 8 (h)), or still the TV method (Fig. 8 (i)) where blocking effect is particularly visible.

Fig. 6. PSNRs in dB (left) and SSIMs (right) as a function of slices of the SR images reconstructed using the EGNI, ZF, TV and LFE methods.
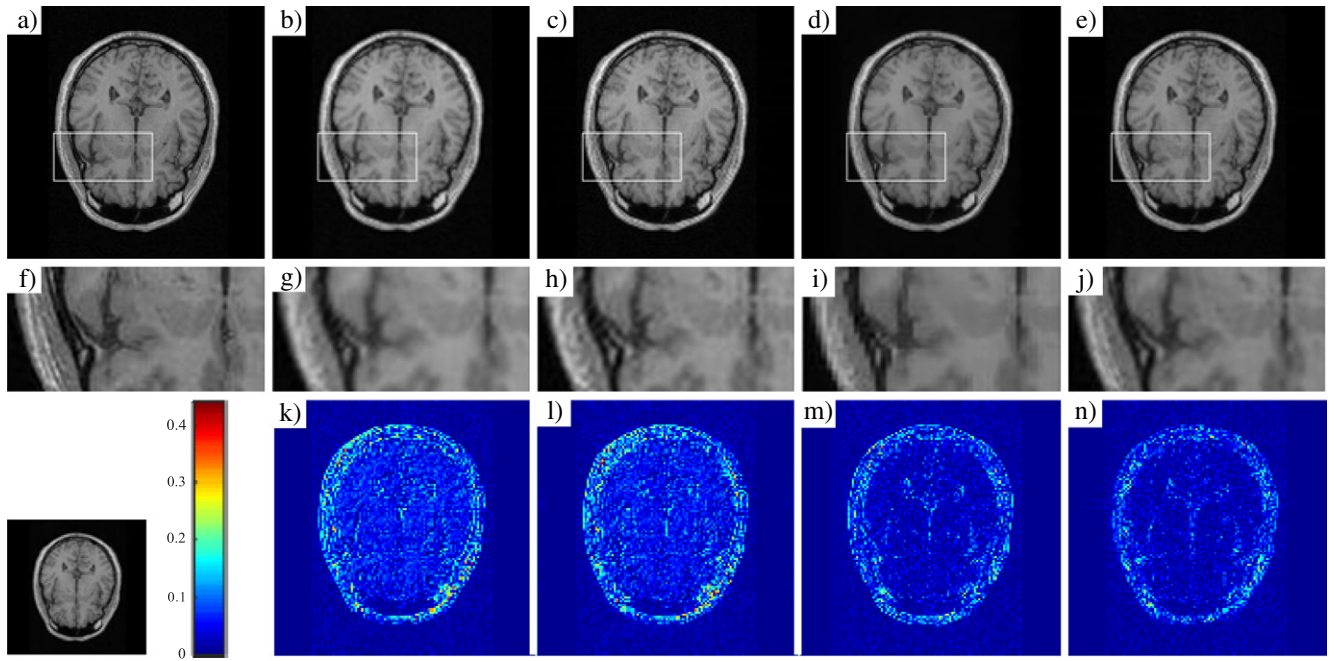
Fig. 7. Super-resolution reconstruction results on the 100th slice reference image. (a) Reference image. (b)–(e) represent the SR images obtained using respectively the EGNI, ZF, TV and LFE methods. (f)–(j) are the zoomed versions of the boxed regions in (a)–(e), respectively. The corresponding image errors between the reconstructed SR images ((b)–(e)) and the reference image ((a)) are given in (k)–(n).
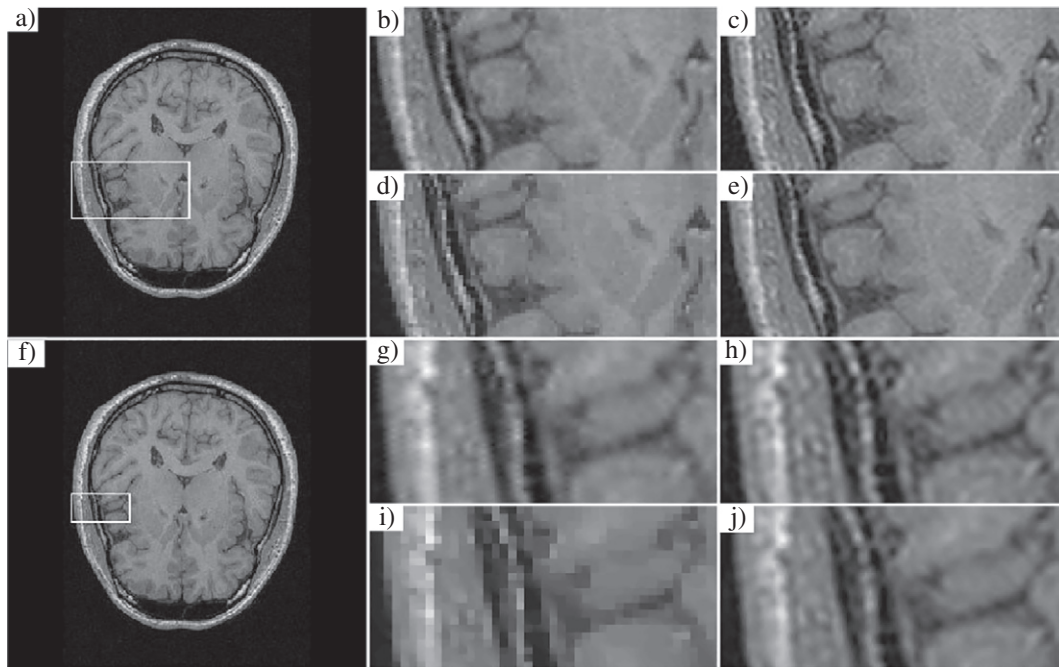
Fig. 8. Super-resolution reconstruction with higher magnification factors. (a) Initial image of size 204 × 176. (b) to (e) represent the regions as boxed in (a) of the SR images with a magnification factor of 2, which were reconstructed using respectively the EGNI, ZF, TV and LFE methods. (f) A smaller boxed region of the same image as in (a). (g) to (j) represent the regions as boxed in (f) of the SR images reconstructed using respectively the EGNI, ZF, TV and LFE methods, which correspond to a magnification factor of 4.

Table 2
Computation time in seconds for the first five SR image experiments.

Methods	1	2	3	4	5
EGNI	39	160	39	159	789
ZF	0.003	0.016	0.004	0.015	0.078
TV	0.86	3.5	0.82	3.5	8.90
LFE	0.003	0.016	0.005	0.018	0.083

Table 2 lists the overall computational efficiency of EGNI, ZF, TV and LFE methods in the first five SR image experiments. All the methods are operated on a PC of Intel Core i5-4460 Quad-Core 3.2 GHz CPU with 4 GB memory. ZF and LFW methods similarly have the fastest computational speed, while the TV method spends less computation time than the EGNI method which runs the most expensive computations.

Table 3
PSNRs and SSIMs for the eight SR image experiments.

Cases	PSNR				SSIM			
	EGNI	ZF	TV	LFE	EGNI	ZF	TV	LFE
1	29.0602	29.3056	30.6283	30.8036	0.9816	0.9817	0.9907	0.9913
2	28.7750	28.9821	29.9099	30.0607	0.9892	0.9880	0.9920	0.9925
3	29.5882	30.0161	31.2284	31.4380	0.9797	0.9815	0.9895	0.9902
4	29.5255	30.0043	31.3300	31.6244	0.9783	0.9815	0.9899	0.9908
5	28.9796	29.1264	30.4487	30.6215	0.9806	0.9782	0.9891	0.9899
6	25.6576	26.3935	29.1219	29.5618	0.9598	0.9685	0.9811	0.9925
7	23.2625	23.6571	26.6679	27.2574	0.8953	0.9132	0.9712	0.9891
8	25.9609	26.7609	28.3118	29.1991	0.9775	0.9844	0.9820	0.9930

Table 3 shows that the LFE method achieves the highest PSNR and SSIM as well as the best performance for all eight volumes whatever the variation of anatomical structures.

We now examine the effect of reconstruction of different SR methods on the consistency of the reconstructed (in the transverse direction) images in the sagittal (Fig. 9 (b)–(e)) and coronal (Fig. 9 (l)–(o)) directions by displaying the reconstructed images in these different directions. It is interesting to note that only the proposed method has preserved the inter-slice consistency in the sagittal and coronal directions. The zoomed versions (Fig. 9 (g)–(j) and (q)–(t)) of the slices (Fig. 9 (b)–(e) and (l)–(o)) clearly show that the EGNI and ZF methods generated visible horizontal strips (Fig. 9 (g)–(h) and (q)–(r)) due to their inherent blurring and ringing artifacts. The TV method yielded blocking artifacts and staircase edges (Fig. 9 (i), (s)). The proposed LFE (Fig. 9 (j), (t)) gave the best highly-resolved detail image with largely reduced ringing artifacts.

4. Discussion and conclusions

The phenomenon of inter-slice inconsistency can be explained as below. Interpolation-based methods (such as EGNI method) produce interpolation errors within in-plane slice (i.e. in transverse slices in the present study), which result in the inconsistency across the sagittal or coronal dimension. The ZF method suffer from severe ringing artifacts within in-plane slice, which leads to important inconsistency in the inter-slice dimension. As for the TV method, the TV-based minimization regularization enforces in general local spatial consistency within in-plane slice and consequently introduces the piecewise blocking artifact visible in the sagittal or coronal direction. In contrast, although also implementing zero-padding in the high frequencies, the proposed LFE method is recovering the low-frequency components of the desired SR image from the k-space of the given LR image whereas windowing k-space data in the ZF method is not
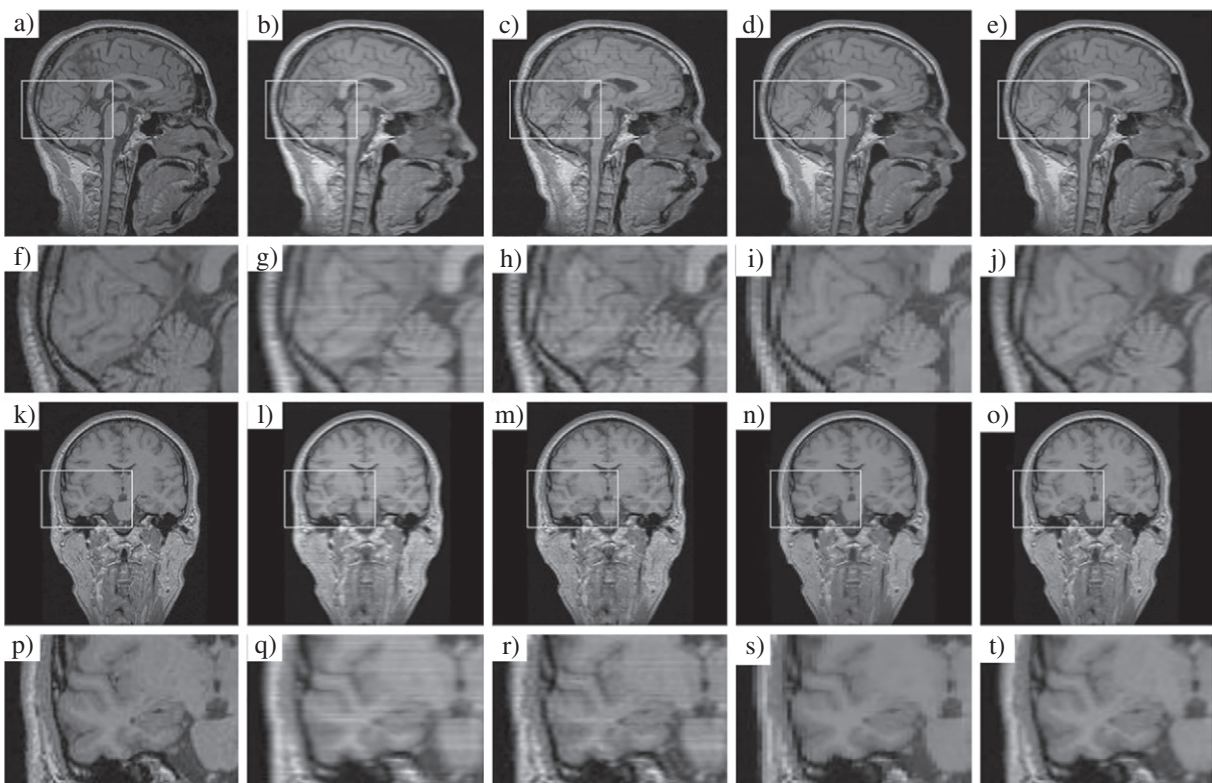
Fig. 9. Transverse super-resolution results displayed in the sagittal and coronal view. (a) Reference image. (b)–(e) represent the sagittal view of the transverse SR images obtained using respectively the EGNI, ZF, TV and LFE methods. (f)–(j) are the zoomed versions of the boxed regions in (a)–(e), respectively. (k) reference image. (l)–(o) represent the coronal view of the transverse SR images obtained using respectively the EGNI, ZF, TV and LFE methods. (p)–(t) are the zoomed versions of the boxed regions in (k)–(o), respectively.

generating any low-frequency components of the desired SR image. This explains why the LFE method yields much higher image quality than the ZF method, which leads to the high spatial consistency of the LFE method in the inter-slice direction. Inversely speaking, the high inter-slice consistency demonstrates the good SR quality of the proposed LFE method.

The results demonstrated that estimating the low-frequency k-space data of the desired SR image from a single spatial modulus LR image is an effective way to obtain a fast, robust and efficient single image SR method allowing achieving not only good in-plane SR image quality but also high inter-slice spatial consistency.

With the proposed SR reconstruction, the resulting super-resolved image is somewhat bandlimited in the sense that the high-frequency k-space is zero-filled. Further improvement could then be achieved if high-frequency k-space data in this k-space can be appropriately recovered. Also, the extension of the proposed SR idea to three-dimensional (3D) images can be envisaged.

Acknowledgments

Appendix

1. The k-space data of the SR image $g(i,j), i,j \in \{0,1,\ldots,sN-1\}$ in the low-frequency space $k_i, k_j \in \left\{-\frac{N}{2}, -\frac{N}{2}+1, \ldots, \frac{N}{2}-1\right\}$ can be expressed as:

$$
\begin{aligned}
G\left(k_i, k_j\right) &= \mathcal{F}\left[g(i,j)\right], \quad k_i, k_j \in \left\{-\frac{N}{2}, -\frac{N}{2}+1, \ldots, \frac{N}{2}-1\right\} \\
&= \sum_{i=0}^{sN-1}\sum_{j=0}^{sN-1} g(i,j) e^{\frac{-2\pi\left(ik_i+jk_j\right)\sqrt{-1}}{sN}} \\
&= \sum_{i=0}^{sN-1} e^{\frac{-2\pi i k_i\sqrt{-1}}{sN}}\left[\sum_{j=0}^{N-1}\left[g(i,sj)e^{\frac{-2\pi sjk_j\sqrt{-1}}{sN}} + \ldots + g\left(i,sj+s-1\right)e^{\frac{-2\pi(sj+s-1)k_j\sqrt{-1}}{sN}}\right]\right] \\
&= \sum_{i=0}^{sN-1} e^{\frac{-2\pi i k_i\sqrt{-1}}{sN}}\left[\sum_{j=0}^{N-1}\left[g(i,sj) + \ldots + g\left(i,sj+s-1\right)e^{\frac{-2\pi(s-1)k_j\sqrt{-1}}{sN}}\right]e^{\frac{-2\pi jk_j\sqrt{-1}}{N}}\right] \\
&= \sum_{i=0}^{sN-1} e^{\frac{-2\pi i k_i\sqrt{-1}}{sN}}\left[\sum_{j=0}^{N-1}\left[\sum_{b=0}^{s-1}g(i,sj+b)e^{\frac{-2\pi bk_j\sqrt{-1}}{sN}}\right]e^{\frac{-2\pi jk_j\sqrt{-1}}{N}}\right] \\
&= \sum_{i=0}^{N-1} e^{\frac{-2\pi si k_i\sqrt{-1}}{sN}}\left[\sum_{j=0}^{N-1}\left[\sum_{b=0}^{s-1}g(i,sj+b)e^{\frac{-2\pi bk_j\sqrt{-1}}{sN}}\right]e^{\frac{-2\pi jk_j\sqrt{-1}}{N}}\right] \\
&\quad + \sum_{i=0}^{N-1} e^{\frac{-2\pi(si+1)k_i\sqrt{-1}}{sN}}\left[\sum_{j=0}^{N-1}\left[\sum_{b=0}^{s-1}g(si+1,sj+b)e^{\frac{-2\pi bk_j\sqrt{-1}}{sN}}\right]e^{\frac{-2\pi jk_j\sqrt{-1}}{N}}\right] \\
&\quad \ldots \\
&\quad + \sum_{i=0}^{N-1} e^{\frac{-2\pi(si+s-1)k_i\sqrt{-1}}{sN}}\left[\sum_{j=0}^{N-1}\left[\sum_{b=0}^{s-1}g\left(si+s-1,sj+b\right)e^{\frac{-2\pi bk_j\sqrt{-1}}{sN}}\right]e^{\frac{-2\pi jk_j\sqrt{-1}}{N}}\right] \\
&= \sum_{i=0}^{N-1} e^{\frac{-2\pi i k_i\sqrt{-1}}{N}}\left[\sum_{j=0}^{N-1}\left[\sum_{b=0}^{s-1}g(si,sj+b)e^{\frac{-2\pi bk_j\sqrt{-1}}{sN}}\right]e^{\frac{-2\pi jk_j\sqrt{-1}}{N}}\right] \\
&\quad + \sum_{i=0}^{N-1} e^{\frac{-2\pi i k_i\sqrt{-1}}{N}}e^{\frac{-2\pi k_i\sqrt{-1}}{sN}}\left[\sum_{j=0}^{N-1}\left[\sum_{b=0}^{s-1}g(si+1,sj+b)e^{\frac{-2\pi bk_j\sqrt{-1}}{sN}}\right]e^{\frac{-2\pi jk_j\sqrt{-1}}{N}}\right] \\
&\quad \ldots \\
&\quad + \sum_{i=0}^{N-1} e^{\frac{-2\pi i k_i\sqrt{-1}}{N}}e^{\frac{-2\pi(s-1)k_i\sqrt{-1}}{sN}}\left[\sum_{j=0}^{N-1}\left[\sum_{b=0}^{s-1}g\left(si+s-1,sj+b\right)e^{\frac{-2\pi bk_j\sqrt{-1}}{sN}}\right]e^{\frac{-2\pi jk_j\sqrt{-1}}{N}}\right] \\
&= \sum_{i=0}^{N-1} e^{\frac{-2\pi i k_i\sqrt{-1}}{N}}\sum_{a=0}^{s-1} e^{\frac{-2\pi ak_i\sqrt{-1}}{sN}}\left[\sum_{j=0}^{N-1}\left[\sum_{b=0}^{s-1}g(si+a,sj+b)e^{\frac{-2\pi bk_j\sqrt{-1}}{sN}}\right]e^{\frac{-2\pi jk_j\sqrt{-1}}{N}}\right]
\end{aligned}
\tag{16}
$$

2. To estimate the k-space data of the desired $G(k_i, k_j)$ in the low-frequency space $k_i, k_j \in \left\{ -\frac{N}{2}, -\frac{N}{2}+1, \ldots, \frac{N}{2}-1 \right\}$ (of size $N \times N$), we replace $g(si + a, sj + b)$ with $a, b \in \{0, 1, \ldots, s-1\}$ and $i, j \in \{0, 1, \ldots, N-1\}$ by its approximate value equal to the pixel value of the LR image $g_l(i, j), i, j \in \{0, 1, \ldots, N-1\}$. The low-frequency k-space data of the SR image $g(i, j)$ can then be approximately expressed as:

$$
\begin{aligned}
G(k_i, k_j) &= \sum_{i=0}^{N-1} e^{\frac{-2\pi i k_i \sqrt{-1}}{N}} \sum_{a=0}^{s-1} e^{\frac{-2\pi a k_i \sqrt{-1}}{sN}} \left[\sum_{j=0}^{N-1} \left[\sum_{b=0}^{s-1} g(si+a, sj+b) e^{\frac{-2\pi b k_j \sqrt{-1}}{sN}} \right] e^{\frac{-2\pi j k_j \sqrt{-1}}{N}} \right] \\
&\approx \sum_{i=0}^{N-1} e^{\frac{-2\pi i k_i \sqrt{-1}}{N}} \sum_{a=0}^{s-1} e^{\frac{-2\pi a k_i \sqrt{-1}}{sN}} \left[\sum_{j=0}^{N-1} \left[\sum_{b=0}^{s-1} g_l(i,j) e^{\frac{-2\pi b k_j \sqrt{-1}}{sN}} \right] e^{\frac{-2\pi j k_j \sqrt{-1}}{N}} \right] \\
&= \sum_{i=0}^{N-1} e^{\frac{-2\pi i k_i \sqrt{-1}}{N}} \sum_{a=0}^{s-1} e^{\frac{-2\pi a k_i \sqrt{-1}}{sN}} \left[\sum_{j=0}^{N-1} \left[g_l(i,j) \sum_{b=0}^{s-1} e^{\frac{-2\pi b k_j \sqrt{-1}}{sN}} \right] e^{\frac{-2\pi j k_j \sqrt{-1}}{N}} \right] \\
&= \left(\sum_{a=0}^{s-1} e^{\frac{-2\pi a k_i \sqrt{-1}}{sN}} \right) \left(\sum_{b=0}^{s-1} e^{\frac{-2\pi b k_j \sqrt{-1}}{sN}} \right) \sum_{i=0}^{N-1} \sum_{j=0}^{N-1} e^{\frac{-2\pi (i k_i + j k_j) \sqrt{-1}}{N}} g_l(i,j) \\
&= \left(\sum_{a=0}^{s-1} e^{\frac{-2\pi a k_i \sqrt{-1}}{sN}} \right) \left(\sum_{b=0}^{s-1} e^{\frac{-2\pi b k_j \sqrt{-1}}{sN}} \right) G_l(k_i, k_j), \quad k_i, k_j \in \left\{ -\frac{N}{2}, -\frac{N}{2}+1, \ldots, \frac{N}{2}-1 \right\}
\end{aligned}
\tag{17}
$$

References

[1] Plenge E, Poot DH, Bernsen M, Kotek G, Houston G, Wielopolski P, van der Weerd L, Niessen WJ, Meijering E. Super-resolution methods in MRI: can they improve the trade-off between resolution, signal-to-noise ratio, and acquisition time? Magn Reson Med 2012;68(6):1983–93.

[2] Ropele S, Ebner F, Fazekas F, Reishofer G. Super-resolution MRI using microscopic spatial modulation of magnetization. Magn Reson Med 2010;64(6):1671–5.

[3] Ning L, Setsompop K, Michailovich O, Makris N, Shenton ME, Westin CF, Rathi Y. A joint compressed-sensing and super-resolution approach for very high-resolution diffusion imaging. NeuroImage 2016;125:386–400.

[4] Nasrollahi K, Moeslund TB. Super-resolution: a comprehensive survey. Mach Vis Appl 2014;25(6):1423–68.

[5] Rueda A, Malpica N, Romero E. Single-image super-resolution of brain MR images using overcomplete dictionaries. Med Image Anal 2013;17(1): 113–32.

[6] Trinh DH, Luong M, Dibos F, Rocchisani JM, Pham CD, Nguyen TQ. Novel example-based method for super-resolution and denoising of medical images. IEEE Trans Image Process 2014;23(4):1882–95.

[7] Velasco NF, Rueda A, Santa Marta C, Romero E. A sparse Bayesian representation for super-resolution of cardiac MR images. Magn Reson Imaging 2017;36:77–85.

[8] Zhang D, He J, Zhao Y, Du M. MR image super-resolution reconstruction using sparse representation, nonlocal similarity and sparse derivative prior. Comput Biol Med 2015;58:130–45.

[9] Manjón JV, Coupé P, Buades A, Fonov V, Collins DL, Robles M. Non-local MRI upsampling. Med Image Anal 2010;14(6):784–92.

[10] Qin B, Shen Z, Zhou Z, Zhou J, Lv Y. Structure matching driven by joint-saliency-structure adaptive kernel regression. Appl Soft Comput 2016;16: 851–67.

[11] Jin M, Li R, Jiang J, Qin B. Extracting contrast-filled vessels in X-ray angiography by graduated RPCA with motion coherency constraint. Pattern Recogn 2017;63:653–66.

[12] Lehmann TM, Gonner C, Spitzer K. Survey: interpolation methods in medical image processing. IEEE Trans Med Imaging 1999;18(11):1049–75.

[13] Dyrby TB, Lundell H, Burke MW, Reislev NL, Paulson OB, Ptito M, Siebner HR. Interpolation of diffusion weighted imaging datasets. NeuroImage 2014;103:202–13.

[14] Zhang L, Wu X. An edge-guided image interpolation algorithm via directional filtering and data fusion. IEEE Trans Image Process 2006;15(8):2226–38.

[15] Deng LJ, Guo W, Huang TZ. Single image super-resolution via an iterative reproducing kernel Hilbert space method. IEEE Trans Circuits Syst Video Technol 2016;26(11):2001–14.

[16] Zhang K, Gao X, Tao D, Li X. Single image super-resolution with non-local means and steering kernel regression. IEEE Trans Image Process 2012;21(11):4544–56.

[17] Jiang J, Chen C, Ma J, Wang Z, Wang Z, Hu R. SRLSP: A face image Super-Resolution algorithm using smooth regression with local structure prior. IEEE Trans Multimedia 2017;19(1):27–40.

[18] Li M, Nguyen TQ. Markov random field model-based edge-directed image interpolation. IEEE Trans Image Process 2008;17(7):1121–8.

[19] Yan Q, Xu Y, Yang X, Nguyen TQ. Single image superresolution based on gradient profile sharpness. IEEE Trans Image Process 2015;24(10):3187–202.

[20] Marquina A, Osher SJ. Image super-resolution by TV-regularization and Bregman iteration. J Sci Comput 2008;37(3):367–82.

[21] Tourbier S, Bresson X, Hagmann P, Thiran JP, Meuli R, Cuadra MB. An efficient total variation algorithm for super-resolution in fetal brain MRI with adaptive regularization. Neuroimage 2015;118:584–97.

[22] Shi F, Cheng J, Wang L, Yap PT, Shen D. LRTV: MR image super-resolution with low-rank and total variation regularizations. IEEE Trans Med Imaging 2015;34(12):2459–66.

[23] Zhang K, Gao X, Li J, Xia H. Single image super-resolution using regularization of non-local steering kernel regression. Signal Process 2016;123:53–63.

[24] Baker S, Kanade T. Limits on super-resolution and how to break them. IEEE Trans Pattern Anal Mach Intell 2002;24(9):1167–83.

[25] Lu X, Huang Z, Yuan Y. MR image super-resolution via manifold regularized sparse learning. Neurocomputing 2015;162:96–104.

[26] Wang YH, Qiao J, Li JB, Fu P, Chu SC, Roddick JF. Sparse representation-based MRI super-resolution reconstruction. Measurement 2014;47:946–53.

[27] Zhang J, Zhang L, Xiang L, Shao Y, Wu G, Zhou X, Shen D, Wang Q. Brain Atlas fusion from high-thickness diagnostic magnetic resonance images by learning-based super-resolution. Pattern Recogn 2017;63:531–41.

[28] Zhang K, Tao D, Gao X, Li X, Xiong Z. Learning multiple linear mappings for efficient single image super-resolution. IEEE Trans Image Process 2015;24(3):846–61.

[29] Kwon Y, Kim KI, Tompkin J, Kim JH, Theobalt C. Efficient learning of image super-resolution and compression artifact removal with semi-local Gaussian processes. IEEE Trans Pattern Anal Mach Intell 2015;37(9):1792–805.

[30] Wang H, Gao X, Zhang K, Li J. Image super-resolution using non-local Gaussian process regression. Neurocomputing 2016;194:95–106.

[31] Liang ZP, Lauterbur PC. Principles of magnetic resonance imaging: a signal processing perspective.2000.

[32] Wang Z, Bovik AC, Sheikh HR, Simoncelli EP. Image quality assessment: from error visibility to structural similarity. IEEE Trans Image Process 2004;13(4):600–12.

[33] Archip N, Clatz O, Whalen S, Kacher D, Fedorov A, Kot A, Chrisochoides N, Jolesz F, Golby A, Black PM, Warfield SK. Non-rigid alignment of pre-operative MRI, fMRI, and DT-MRI with intra-operative MRI for enhanced visualization and navigation in image-guided neurosurgery. Neuroimage 2007;35(2):609–24.